Climate Dynamics (2022) 59:869–886
https://doi.org/10.1007/s00382-022-06161-z

Association of the shift of the South Asian high in June with the diabatic heating in spring

Shu Gui[1] · Qin Su[1] · Ruowen Yang[1] · Jie Cao[1]

Received: 19 August 2021 / Accepted: 18 January 2022 / Published online: 12 February 2022

Abstract
In this paper, we define the index of the South Asian High (SAH) core position and use correlation analysis and ERA-Interim reanalysis data during 1979–2018 to identify spring latent heating configurations in the central Indian Ocean–southwestern Tibetan Plateau that provide leading signals for the SAH shift in June via the apparent moisture sink. These leading signals in boreal spring have a clear physical significance, and are characterized by a contrast in the meridional apparent moisture sink between the central Indian Ocean (IO) and the southwestern Tibetan Plateau (SWTP). When the spring apparent moisture sink contrast between the central IO and the SWTP is higher than normal, the heating pattern induces an anomalous vertical circulation that enhances the coupling between the mid-level convection and upper-level divergence over the central IO-SWTP. The upper-level divergent circulation in the upper reaches of the SAH track favors the development of the SAH before June, and thus the SAH shifts farther northwestward than normal in June. When the spring apparent moisture sink contrast is lower than normal, the atmospheric response is reversed, causing the SAH to shift farther southeastward than normal. Numerical experiments have confirmed the driving role of the meridional apparent moisture sink contrast in the central IO-SWTP and the associated physical processes. Further analyses reveal a significant and persistent correlation between the apparent moisture sink contrast in late March to late May and the SAH meridional position in June. The spring meridional apparent moisture sink contrast is therefore a reasonable predictor in forecasting the SAH shift in June.

Keywords South Asian High · Apparent moisture sink · Leading signals

1 Introduction

The South Asian High (SAH), a huge semi-permanent anticyclone in the upper troposphere, is one of the most important components of the Asian Summer Monsoon (ASM) system (Tao and Chen 1987). Variations in its magnitude and displacement significantly modulate the weather and climate over Asia. For example, a stronger SAH causes more rainfall in southern Asia and less over the Yangtze River Valley (YRV) and the Pacific Ocean (Zhang et al. 2005; Wei et al. 2015). Stronger Tibetan and Iranian modes of the SAH are usually related to cold and wet surface anomalies in Mongolia and northern China, whereas weaker modes lead to dry and warm anomalies (Shi and Qian 2016). The eastward shift of the SAH may increase rainfall in Korea and favor intense Meiyu precipitation over the YRV, whereas the northwest shift of the SAH can cause more extreme precipitation in the northern part of eastern China but less over the Yangtze-Huai River Basin (Choi et al. 2015; Ning et al. 2017; Yin et al. 2020). A more westward position of the SAH leads to enhanced rainfall over India and weakened rainfall over the western Pacific, and the opposite is observed when the SAH is farther eastward (Nützel et al. 2016). A stronger SAH in April causes an earlier onset of the Meiyu rains and more precipitation in June over the YRV (Li et al. 2019). Besides the influence that rainfall anomalies have on seasonal and monthly precipitation scales, the 10–20-day oscillation in the SAH also has an important impact on rainfall over the YRV 3 days later (Wei et al. 2019). Thus, a better understanding of the key physical processes in the variations of the SAH will improve the accuracy of weather and climate forecast.

✉ Ruowen Yang
yangruowen@ynu.edu.cn

✉ Jie Cao
caoj@ynu.edu.cn

[1] Department of Atmospheric Sciences, Yunnan University, Kunming 650091, China

Previous studies have addressed the importance of synchronous diabatic heating in understanding variations in the SAH. The SAH is principally related to convection processes during the southwest monsoon season (Krishnamurti et al. 1973). Specifically, heating over the Tibetan Plateau (TP) during the transition season from winter to summer plays an important role in the movement and development of the SAH (Reiter and Gao 1982). Precipitation related to the ASM also contributes to the formation and movement of the SAH via latent heating (Liu et al. 2001, 2013; Wu and Liu 2003; Liu and Wu 2004; Wei et al. 2013; Zhang et al. 2015). Strong latent heating from deep convection induces strong updrafts and upper-level divergence that causes the SAH to become fully established over the Indochina Peninsula in mid-May (Wang et al. 2017).

In comparison to the heating over the TP, the ASM heating may have a greater influence on the northward movement of the SAH (Ge et al. 2018b). Zhang et al. (2019a) suggested that enhanced latent heat released over northeastern India in May causes the northwestward shift of the SAH in June. There is also a robust relationship between the variation in the SAH and ASM-related heating on subseasonal timescales. For example, the variation in the SAH is closely related to transient deep convection on a 10–20-day timescale over Southeast Asia (Randel and Park 2006). A reduction in rainfall over northern India occurs ~ 1 day ahead of the eastward movement of the SAH on a quasi-biweekly timescale (Wei et al. 2019).

In addition to ASM-related heating, the sea surface temperature (SST) anomalies of the IO and the Pacific Ocean play an important role in modulating the SAH. For example, the tropical Indian Ocean (IO) SST anomalies alter the equivalent potential temperature in the atmospheric boundary layer and produce significant geopotential height anomalies that modulate the SAH (Huang et al. 2011; Zhang et al. 2020). The influence of the tropical IO on the intensity of the SAH became more important after the late 1970s (Qu and Huang 2012). Previously, El Niño-Southern Oscillation events in the easterly phase of the boreal winter quasi-biennial oscillation exerted more impact on the intensity of the SAH via moist adjustment (Xue et al. 2015, 2017; Zhang et al. 2019b). The summer SAH tends to be stronger when an El Niño occurs with a positive phase of the Pacific decadal oscillation, and weaker when a La Niña occurs with a negative phase of the Pacific decadal oscillation (Xue et al. 2018). Xue and Chen (2019) found that the overall mode of the SAH is controlled by a combination of anomalous rainfall over the Indian Peninsula and SST anomalies over the IO.

Most previous studies that discussed latent heat release have focused on the relationship between the intensity of the summer SAH and concurrent convection processes. For example, the zonal shift of the SAH was affected by anomalous latent heating associated with the ISM variability and the summer rainfall in China (Raman and Rao 1981; Krishnamurti et al. 1989; Zhang and Wu 2001; Zhou et al. 2006; Wei et al. 2013). Specifically, the latent heat release in the YRV has a feedback effect on the SAH shift by exciting an upper-level anticyclone over eastern China (Wei et al. 2015). The meridional shift of the SAH is closely associated with the initiation of convection over Indo-Chinese Peninsula, northward migration of convection over Sumatra, and the tripolar pattern of summer rainfall anomalies in China (He et al. 2006; Wei et al. 2012). The northward movement of the SAH is affected more by the Asian summer monsoon heating than the diabatic heating of Tibetan Plateau (Ge et al. 2018b).

June is the key month when the SAH shifts onto the TP (Zhu et al. 1980). If a leading signal for the northward shift of the SAH in June can be identified, they can potentially improve the forecasting of summer droughts or floods over the region affected by the ASM. It is therefore important to extract the leading signals for the northward shift of the SAH in June, and further explore the corresponding physical processes. Since the heat preference of the SAH can be revealed via the atmospheric apparent heat source and apparent moisture sink (Wang and Qian 2000; Qian et al. 2002; Cen et al. 2020), we searched the leading signals from these two diabatic heating variables.

The remainder of this study is organized as follows. The data, method, and atmospheric general circulation model (AGCM) are described in Sect. 2. An index for the core position of the SAH is constructed in Sect. 3. Section 4 describes the extraction of leading signals and investigates their relationship to the SAH meridional position in June. The possible physical processes behind this relationship are discussed in Sect. 5. Section 6 shows the persistence of the significant correlation between diabatic heating, zonal wind, and meridional position of the SAH in June. Model results are presented in Sect. 7 to confirm the relationship outlined in Sect. 6, and the physical processes associated with it, that were obtained in Sects. 4–6. A summary is presented in Sect. 8.

2 Data and methods

2.1 Data

The ERA-Interim reanalysis data is used due to its relatively good representability over the research domain and the broad applications of its preceding ERA-Interim data in the studies of atmospheric heat source (Dee et al. 2011; Wu et al. 2015; Cheng et al. 2018; Wang et al. 2019; Han et al. 2021; Zhang et al. 2021). The data resolution is 0.25°

in longitude and latitude on 37 pressure levels from 1000 to 1 hPa for all variables during the period 1979–2018.

2.2 Method

2.2.1 Apparent heat source and apparent moisture sink

The apparent heat source (Q_1) and apparent moisture sink (Q_2) are calculated from the daily ERA-Interim reanalysis data using the thermodynamic Eq. (1) and the water vapor Eq. (2), respectively.

$$Q_1 = C_p\left(\frac{p}{p_0}\right)^{\kappa}\left(\frac{\partial\theta}{\partial t} + \vec{V}\cdot\nabla\theta + \omega\frac{\partial\theta}{\partial p}\right) \tag{1}$$

$$Q_2 = -L\left(\frac{\partial q}{\partial t} + \vec{V}\cdot\nabla q + \omega\frac{\partial q}{\partial p}\right) \tag{2}$$

The two equations above are the same as in Yanai et al. (1992). In Eqs. (1) and (2), $\vec{V}$ is horizontal velocity, θ is potential temperature, ω is vertical velocity at the isobaric surface, q is the mixing ratio of water vapor, ∇ is the isobaric gradient operator, t is time, p is pressure, $p_0 = 1000$ hPa, C_p is the specific heat at constant pressure of dry air, $\kappa = R/C_p$, R is the gas constant of dry air, and L is the latent heat of condensation.

The column-integrated apparent heat source and apparent moisture sink are calculated as follows:

$$\langle Q_1\rangle = \frac{1}{g}\int_{p_t}^{p_s} Q_1 dp \tag{3}$$

$$\langle Q_2\rangle = \frac{1}{g}\int_{p_t}^{p_s} Q_2 dp \tag{4}$$

where $p_t = 1000$ hPa, and p_s is the surface pressure.

2.2.2 Decomposition of vertical velocity

Under the quasi-geostrophic framework, the vertical velocity can be decomposed into three terms (Eq. 5), i.e. the isentropic gliding component (ω_{IG}), the isentropic displacement component (ω_{ID}) and the diabatic heating component (ω_Q) (Wu et al. 2020).

$$\omega = \omega_{ID} + \omega_{IG} + \omega_Q \tag{5}$$

$$\omega_{ID} = -\Theta_p^{-1}\left(\frac{\partial\theta}{\partial t}\right) \tag{6}$$

$$\omega_{IG} = -\Theta_p^{-1}\overrightarrow{V_g}\cdot\nabla\theta \tag{7}$$

$$\omega_Q = \Theta_p^{-1}\dot{\theta} \tag{8}$$

where Θ_p is the vertical gradient of the standard potential temperature averaged over the research domain and the research period, θ is potential temperature, $\vec{V}_g$ is the geostrophic wind, ∇ is the isobaric gradient operator, $\dot{\theta}$ represents the diabatic heating rate. Thus, ω_{ID} represents the forcing of potential temperature tendency, ω_{IG} represents the forcing of potential temperature advection, and the ω_Q represents the forcing of diabatic heating. The other methods adopted in this study include correlation analysis and the corresponding Student's t-test.

2.3 Numerical model

We also use the atmospheric model ECHAM (version 6.3.05p2, hereafter ECHAM6) to verify the physical processes associated with the diabatic heating anomalies preceding the northward shift of the SAH in June. ECHAM6 is developed by the Max Planck Institute of Meteorology (MPI; Stevens et al. 2013). The ECHAM6 model has been successfully applied in many climate change studies (Cao et al. 2016; Rackow et al. 2018; Nordling et al. 2019; Yang et al. 2019; Gui et al. 2020; Ma and Jiang 2020). There have been multiple updates of the physics in ECHAM6 over previous releases of the model, such as the surface albedo (Roeckner et al. 2012), dynamic vegetation (Reick et al. 2013), radiative transfer, and mid-atmospheric processes (Stevens et al. 2013). In this study, the spatial resolution of ECHAM6 is set to T63L47 (equivalent to 1.875° on a Gaussian grid, and 47 hybrid sigma-pressure levels in the vertical direction). The major physical parameterizations take their default settings, such as the standard RRTM radiation scheme with a diurnal cycle (Mlawer et al. 1997), the TIEDTKE cumulus scheme with modifications from Nordeng (1994), and the aerosol climatology compiled by Kinne et al. (2013). The monthly SST and sea ice extent climatology are used as boundary conditions. Each experiment has been configured to integrate 31-year realizations, and the last 30 years of simulation results are used for analysis.

3 Index for the core position of the SAH

In a similar approach to the definition of the westward ridge point variability of the Western Pacific Subtropical High (Yang et al. 2017), the ridge line of the SAH is also defined as a line with zero zonal wind, westerly wind north of the line, and easterly south of the line. The SAH Core Position Index (SAHCPI) is defined as the point on the ridge

line of the SAH at maximum geopotential height at 100 hPa in June. Specifically, the zero-line of zonal wind is calculated to identify the ridge line and then the location of the maximum geopotential height on the ridge line is defined as the SAHCPI. Thus, SAHCPI is two-dimensional, reflecting the zonal and meridional shift of the SAH's core. Here, we denote the index associated with the meridional shift of the SAH as the Meridional-SAHCPI (M-SAHI), and the index associated with the zonal shift of the SAH as the Zonal-SAHCPI (Z-SAHI). Figure 1a shows the climatological position of the SAH's core from May to August. The SAH's core lies over the northwestern Indochina Peninsula in May. The core jumps ~ 6° northward onto the TP in June, shifts northwestward to the western edge of the TP in July, and retreats slightly eastward in August. The core position of the SAH reflected by the SAHCPI in May–August is similar to that found in previous studies (Luo et al. 1982; He et al. 2006), indicating that the SAHCPI defined above is reasonable. Figure 1b, c shows that the shift of the SAH's core position in the meridional direction has pronounced interannual variability. In fact, the power spectral density of M-SAHI has a significant peak at the 95% confidence level on the quasi-triennial period.

4 Relationship between the apparent moisture sink configuration and the SAH movement in June

We calculated the correlation between the June M-SAHI and the $\langle Q_1 \rangle$ and $\langle Q_2 \rangle$ in April and in May in order to explore the relationship between the configuration of spring diabatic heating over the Indian Ocean–Tibetan Plateau and the interannual variability of the SAH's core position in June. Figure 2a shows that there is a significant positive correlation between the June M-SAHI and April $\langle Q_1 \rangle$ over the southeastern Arabian Sea (AS) as far as the southeastern Bay of Bengal (BOB). Over the Tibetan Plateau, there is a west to east pattern of negative–positive–negative coefficients. In comparison with that shown in Fig. 2a, there is a more regular, banded distribution of correlation coefficients between the June M-SAHI and April $\langle Q_2 \rangle$ (Fig. 2b). The southern AS-southeastern BOB is characterized by significant positive correlation coefficients, and the western-middle Tibetan Plateau is dominated by significant negative correlation coefficients. The patterns in correlation coefficients between the June M-SAHI and the diabatic heating in May resemble those in April. There is a significant positive correlation between the June M-SAHI and May $\langle Q_1 \rangle$ across the southern AS-southeastern Tibetan Plateau, with a negative correlation in the middle of the Tibetan Plateau (Fig. 2c). The distribution of correlation coefficients between the June M-SAHI and May $\langle Q_2 \rangle$ (Fig. 2d) more closely resembles

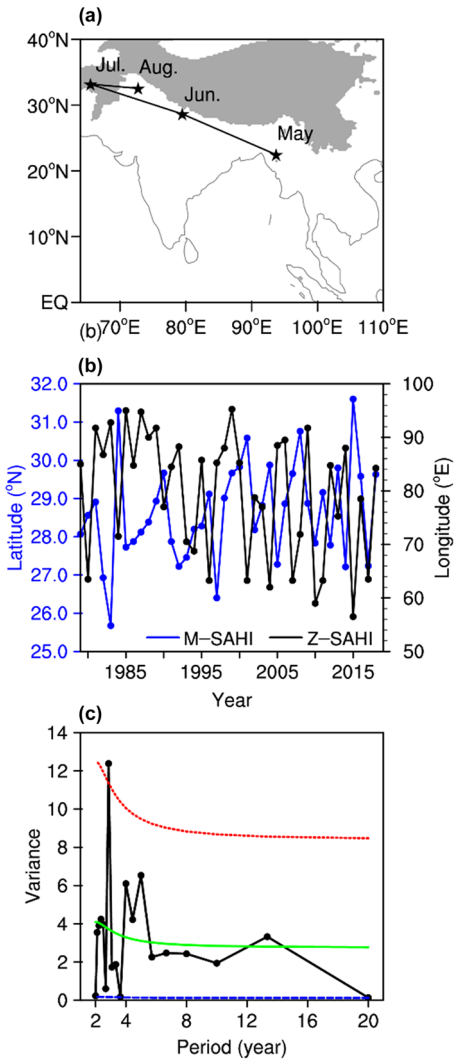

Fig. 1 **a** Location of the SAH core position (asterisk) and climatological track of the SAH (line) in May–August, **b** the meridional index of the SAH (M-SAHI, blue line) and the zonal index of the SAH (Z-SAHI, black line)in June during 1979–2018, and **c** power spectral density of the M-SAHI with the Markov red noise spectrum (solid green line) and its confidence bound at the 95% (dashed red line) and 5% (dashed blue line) levels. The gray area in (**a**) denotes the surface elevation threshold at 850 hPa

that in Fig. 2b. The southern AS-eastern BOB is characterized by a significant positive correlation between the June M-SAHI and May $\langle Q_2 \rangle$. The main difference between April and May is that significant positive correlation coefficients appear over the northeastern BOB-southeastern Tibetan Plateau with values at the center of this region exceeding 0.4 in May. A possible reason for this difference is the location of the SAH's core around the northwestern Indochina Peninsula (Fig. 1a), which will have a divergence pumping effect coupled with strong mid-tropospheric ascent (Liu et al. 2013). The correlation over the northern BOB–Indochinese Peninsula is much higher in May than in April,

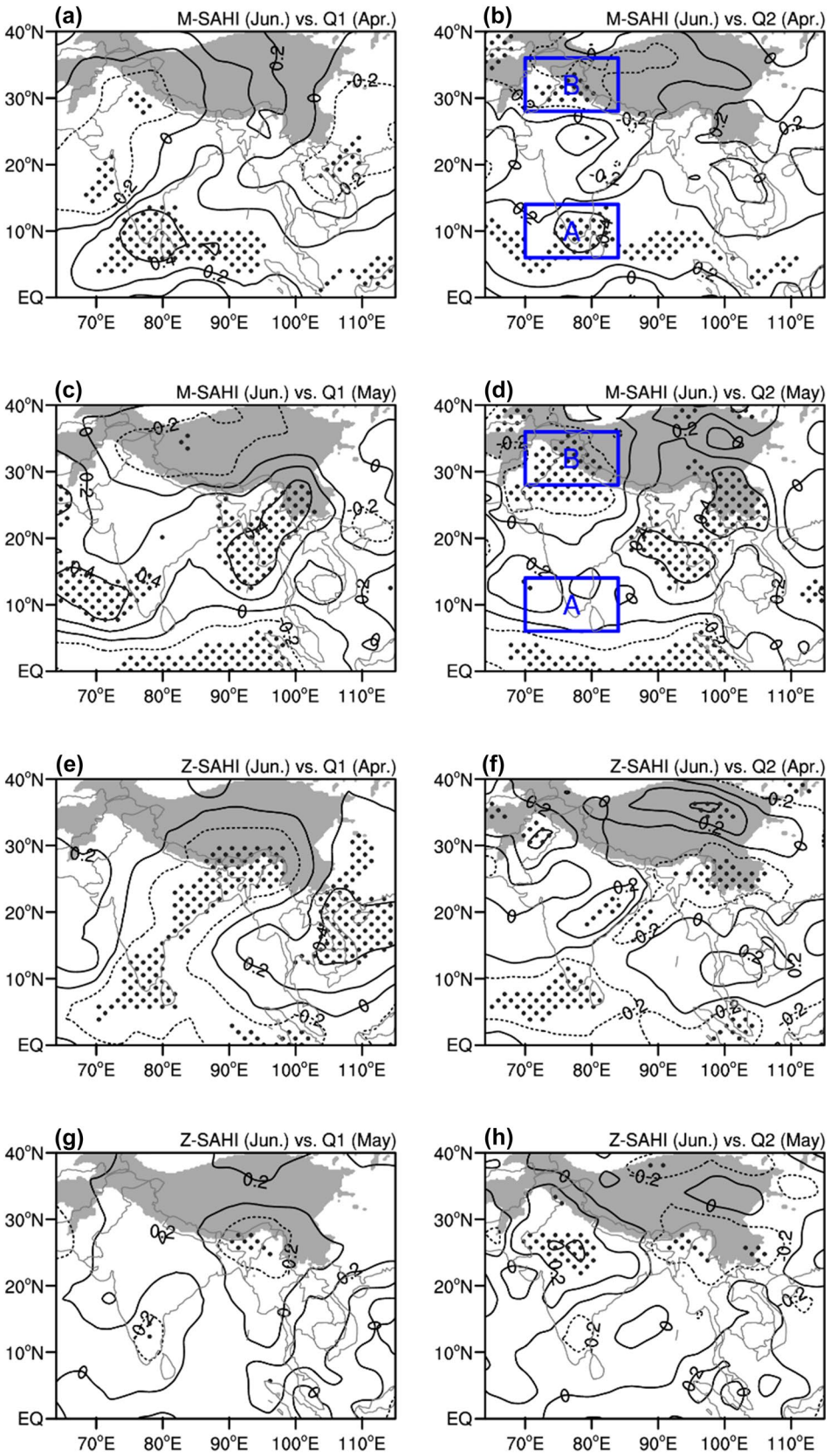

Fig. 2 Correlations between the M-SAHI and **a** apparent heat source in April, **b** apparent moisture sink in April, **c** apparent heat source in May, and **d** apparent moisture sink in May. Panels **e**–**h** are the same as **a**–**d** except for the Z-SAHI. Dots denote the areas of 95% significance based on the Student's *t* test. The surface elevation threshold at 850 hPa is shaded in gray in each plot. Rectangle A and Rectangle B denote the two key areas of the apparent moisture sink

which is closely related to the SAH being established over the Indochinese Peninsula in May (Fig. 1a). This signal over the northern BOB–Indochinese Peninsula should be considered as more of a concurrent signal than a preceding signal. When the SAH shifts to the SWTP, this concurrent signal is reinforced and it replaces the preceding signal over the central IO-SWTP (Fig. S1).

The correlation patterns of the Z-SAHI, $\langle Q_1 \rangle$ and $\langle Q_2 \rangle$, also show a meridional heating contrast but with opposite signs to the M-SAHI; i.e., there are negative anomalies over the central IO and positive anomalies over the SWTP (Fig. 2e–h). This could be because the zonal and meridional shift of the SAH are significantly correlated with each other (Wei et al. 2015). As the centers of high correlation remain in the same area in April and May, the diabatic heating averaged in rectangle A (6°–14°N, 70°–84°E) and B (28°–36°N, 70°–84°E) could be taken as the key signal for the northward shift of the SAH in June. In order to eliminate the differences in variance between the two regions, we constructed a diabatic heating index by normalizing the areal average diabatic heating variables over each region, and calculated the correlation coefficients of the M-SAHI, Z-SAHI and the diabatic heating indices (Table 1). If only rectangle A is considered, the correlation between the M-SAHI and the normalized $\langle Q_2 \rangle$ is statistically insignificant in May. If only rectangle B is considered, the correlation between the M-SAHI and the normalized $\langle Q_1 \rangle$ is statistically insignificant in both April and May. The correlation coefficients only remain significant for both $\langle Q_1 \rangle$ and $\langle Q_2 \rangle$ if the diabatic heating contrast between rectangle A and B is considered. As the apparent moisture sink contrast (AMSC) is most strongly correlated with the M-SAHI, we define the apparent moisture sink contrast index (AMSCI) as follows (Eq. 5):

$$\mathrm{AMSCI} = \left[Q_2(6°-14°\mathrm{N}, 70°-84°\mathrm{E})\right] - \left[Q_2(28°-36°\mathrm{N}, 70°-84°\mathrm{E})\right] \quad (5)$$

In Eq. (5), square brackets denote the normalization by standard deviation, and parentheses denote the average over the specified region. The AMSCI calculated with Eq. (5) is shown for April and May in Fig. 3. The correlation coefficient between the AMSCI and the M-SAHI is 0.60 in April and 0.49 in May, both of which are statistically significant above the 99% confidence level. The correlation coefficient between the AMSCI and M-SAHI is higher than between the AMSCI and Z-SAHI (Table 1). Therefore, the AMSCI in spring can potentially serve as a preceding signal for the northward shift of the SAH in June.

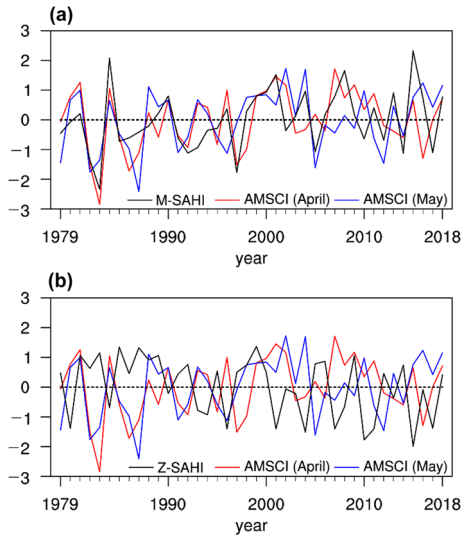

Fig. 3 Time series of **a** the normalized M-SAHI in June and the normalized AMSCI in April and May, **b** the normalized Z-SAHI in June and the normalized AMSCI in April and May. The dash line denotes the zero line

5 Possible physical processes

The apparent moisture sink over the research domain was first regressed onto the AMSCI to obtain the apparent moisture sink distribution associated with the AMSCI. When the AMSCI is higher than normal in April, a positive band of the column-integrated apparent moisture sink $\langle Q_2 \rangle$ almost dominates the tropical North IO, and a negative $\langle Q_2 \rangle$ band controls most of the southern TP (Fig. 4a). These two anomalous patterns remain significant throughout the troposphere with a positive center in the lower troposphere and a negative center in the middle troposphere (Fig. 4b).

Table 1 Correlation coefficients between the SAHI and the normalized diabatic heating index averaged in rectangle A and B

Region	April			May		
	A	B	A–B	A	B	A–B
$\langle Q_1 \rangle$ and M-SAHI	0.51**	−0.25	0.53**	0.33*	−0.20	0.35*
$\langle Q_2 \rangle$ and M-SAHI	0.54**	−0.39*	0.60**	0.18	−0.55**	0.49**
$\langle Q_1 \rangle$ and Z-SAHI	−0.47**	0.08	−0.39*	−0.13	0.11	−0.16
$\langle Q_2 \rangle$ and Z-SAHI	−0.37*	0.33*	−0.46**	−0.16	0.33*	−0.33*

Superscript * denotes correlation coefficients passing the significance test at the 95% confidence level, and ** denotes correlation coefficient passing the significance test at the 99% confidence level

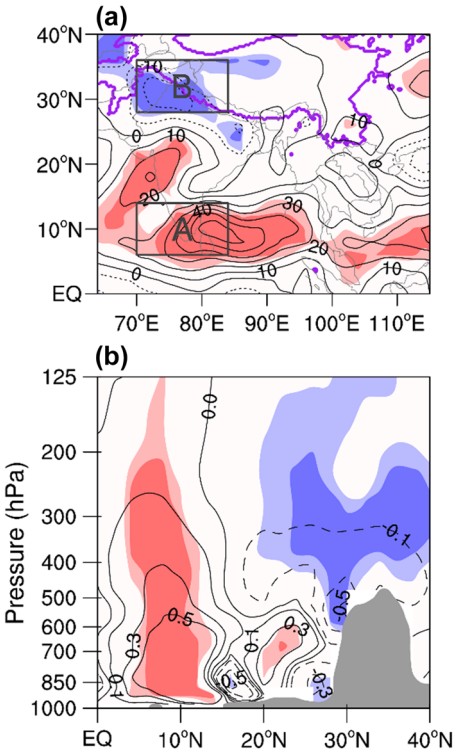

Fig. 4 Regression results of **a** the column-integrated apparent moisture sink, and **b** the apparent moisture sink along 80°E against the normalized AMSCI in April (contour units: W/m^2). The light and dark shadings denote the 95% and 99% significance based on the Student's *t* test, and the blue and red shadings are for negative and positive regression coefficients, respectively. In Panel **a**, rectangle A and B denote the two key areas of the apparent moisture sink, and the purple contour represents the surface elevation threshold at 850 hPa. In Panel **b**, the gray area in (**b**) denotes the surface elevation

The higher-than-normal apparent moisture sink over the central IO induces significant negative geopotential height anomalies at 850 hPa south of 20°N (Fig. 5a), and a lower-than-normal apparent moisture sink over the SWTP induces significant positive geopotential height anomalies at 100 hPa north of 20°N (Fig. 5b). The anomalous divergent wind patterns are consistent with the geopotential height anomalies. In the lower troposphere, divergent northwesterly anomalies north of 10°N converge with divergent southwesterly anomalies south of 10°N over the central IO (Fig. 5c). In the upper troposphere, anomalous divergent easterly winds prevail over the TP (Fig. 5d). As the reference point (24°N, 80°E) is on the pathway of the SAH moving to the TP (Fig. 1a), we draw two sections across this point. The AMSC anomalies induce an anomalous clockwise circulation in the pressure-latitude section, and an anomalous anti-clockwise circulation in the pressure-longitude section (Fig. 5e, f). In the pressure-latitude section (Fig. 5e), anomalous ascending motions occur around 10°N, anomalous southerly divergent winds prevail over the upper troposphere from 10°N to 30°N, anomalous descending motions occur around 30°N, and anomalous northerly divergent winds appear over the lower troposphere from 20°N to 30°N. In the pressure-longitude section (Fig. 5f), anomalous descending motions occur west of 80°E, anomalous westerly divergent winds mostly prevail over the lower-middle troposphere between 80°E and 90°E, anomalous ascending motions generally occur around 100°E, and anomalous easterly divergent winds prevail over the upper troposphere between 70°E and 100°E. Upper-level divergence, indicated by negative velocity potential, favors the development and northwestward shift of the SAH, consistent with the anomalous zonal and meridional vertical circulation.

The AMSC pattern persists in May with a positive center over the central IO and a negative center over the SWTP (Fig. 6a, b). This anomalous AMSC pattern modulates atmospheric circulation to favor the northward shift of the SAH (Fig. 7). The geopotential height anomalies in May tend to move farther westward than those in April (Fig. 7a, b). In particular, the negative geopotential height anomalies in the lower troposphere are west of the Indo-Chinese Peninsula, and the positive geopotential height anomalies in the upper troposphere are west of the TP. The anomalous divergent wind is also consistent with the geopotential height patterns (Fig. 7c, d). The upper-level divergence over South Asia is considerably intensified in May owing to the persistent modulation of the AMSC. The vertical cross-sections show stronger ascending motions associated with stronger upper-level divergence than in April (Fig. 7e, f). Substantial divergent southerly and easterly anomalies remain in the upper troposphere.

To verify the roles of AMSC forcing on the SAH movement, we regressed the large-scale circulation in June against the AMSCI in April (Fig. 8). The geopotential field shows prominent negative anomalies in the lower troposphere over the SWTP, associated with positive anomalies in the upper troposphere (Fig. 8a, b). This pattern indicates a lower-level convergence and upper-level divergence configuration around the SWTP. The spatial pattern of velocity potential also shows an enhanced low-level convergence associated with upper-level divergence over the SWTP (Fig. 8c, d). To explore the vertical structure of the circulation response, the same reference point (24°N, 80°E) is selected around the center of velocity potential anomalies in Fig. 8c, d. The pressure-latitude cross-section shows anomalous ascent in between 15°N and 35°N, associated with significant lower-level convergence and upper-level divergence (Fig. 8e). The pressure-longitude cross-section also exhibits significant ascending anomalies that bridge the low-level convergence and upper-level divergence across the research domain (Fig. 8f). The regression against the AMSCI in May shows a similar pattern (figure omitted). The above results indicate that positive AMSCI configuration is associated with

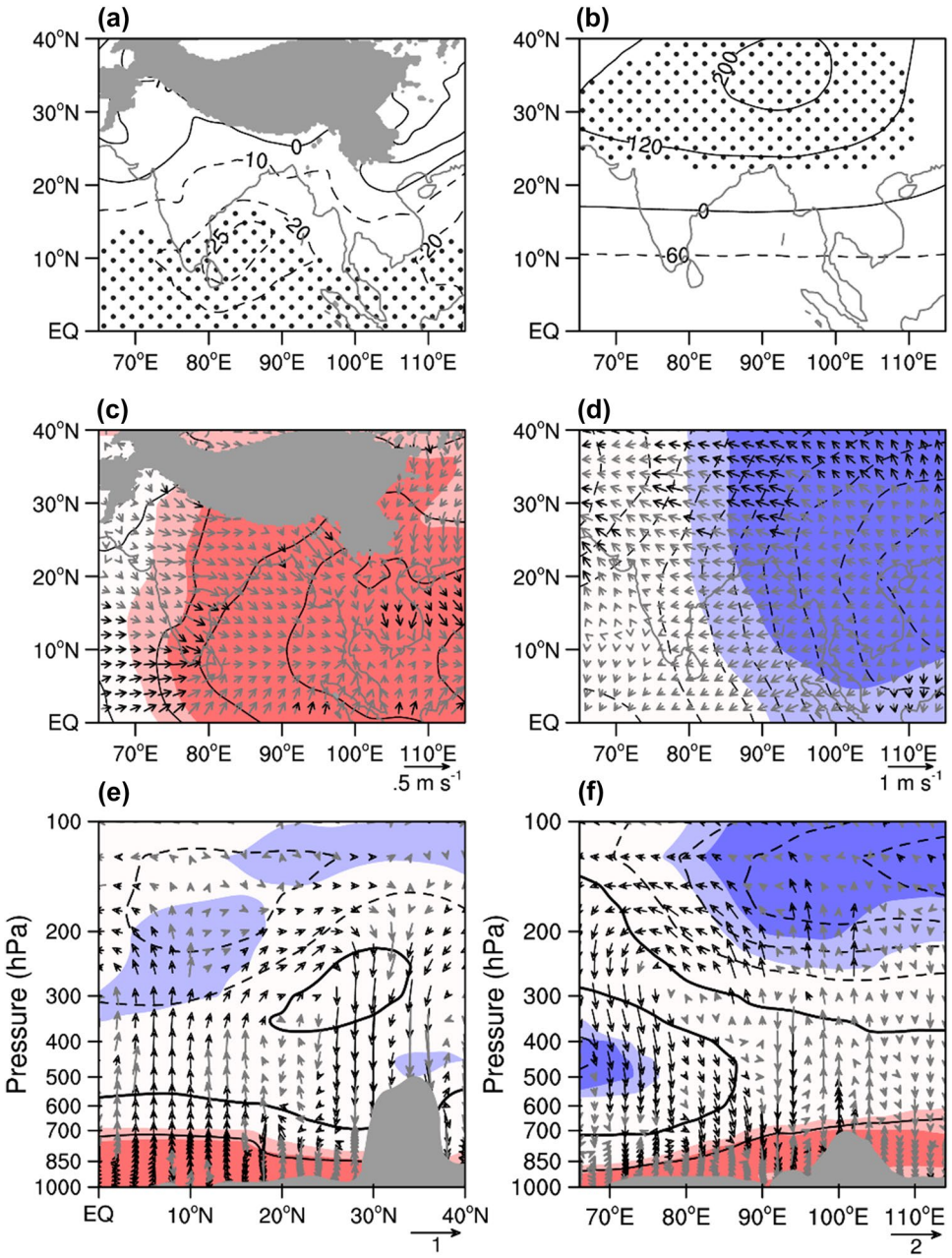

Fig. 5 Regression results of geopotential height at **a** 850 hPa and **b** 100 hPa, divergent winds at **c** 850 hPa and **d** 100 hPa, vertical divergent circulation (vector, vertical velocity is multiplied by 100) and velocity potential (contour, units: 3×10^5 m^2 s^{-1}) along **e** 80°E and **f** 24°N against the normalized AMSCI in April. The stippling in panels **a** and **b**, and the bold arrows in panels **c**–**f** denote the 95% significance based on the Student's *t* test. In panels **c**–**f**, the light and dark shadings denote the 95% and 99% significance based on the Student's *t* test, where the blue and red shadings are for negative and positive regressions coefficients, respectively. The gray areas in (**a**) and (**c**) denote the elevation threshold at 850 hPa, and the gray areas in (**e**) and (**f**) denote the surface elevation

enhanced coupling between the mid-level convection and the upper-level SAH (a.k.a. divergence pumping effect), and vice versa.

The impact mechanism of the AMSC could be revealed by the vertical velocity decomposition. The anomalous AMSC heating causes significant air ascent over the central IO and air descent over the SWTP in April (Fig. 9a). The strong meridional clockwise circulation associated with mid-level southerly anomalies (Fig. S2d) brings warm potential temperature advection to the SWTP, causing the local potential temperature to rise. The warm potential temperature advection results in descending ω_{IG} anomalies and the positive potential temperature tendency causes descending ω_{ID} anomalies (Fig. 9b, c). The combined effect of the three vertical velocity components is to enhance the upward motion over the IO and intensify the downward motion over the SWTP (Fig. 9d). The AMSC forcing in May shows stronger positive anomalies over the central IO than in April (Figs. 4, 6), which further enhances the local ω_Q ascending anomaly (Fig. 9e). The strong low-level convergence associated with northerly anomalies (Fig. S2h) brings cold potential temperature advection and results in ascending ω_{IG} anomalies (Fig. 9f). The negative potential temperature tendency resulted from the cold temperature advection induces ascending ω_{ID} anomalies (Fig. 9g). The combined effect of the three vertical velocity components

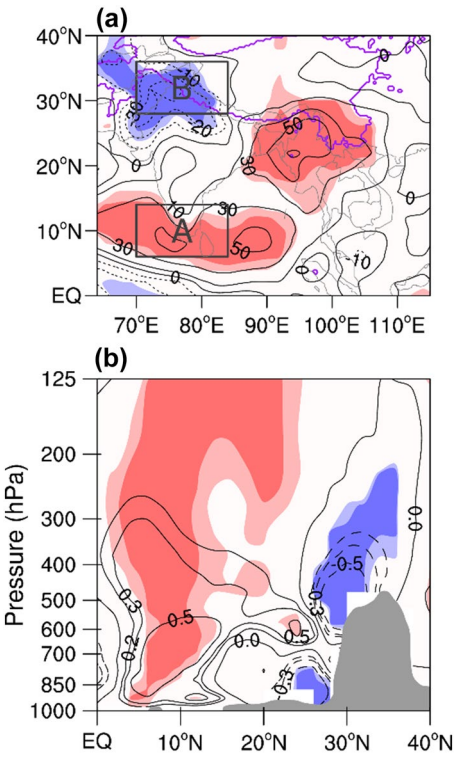

Fig. 6 Regression results of **a** the column-integrated apparent moisture sink, and **b** the apparent moisture sink along 80°E against the normalized AMSCI in May (contour units: W/m^2). The light and dark shadings denote the 95% and 99% significance based on the Student's *t* test, and the blue and red shadings are for negative and positive regression coefficients, respectively. In Panel **a**, rectangle A and B denote the two key areas of the apparent moisture sink, and the purple contour represents the surface elevation threshold at 850 hPa. In Panel **b**, the gray area in (**b**) denotes the surface elevation

is to enhance the upward motion over the central IO and the downward motion over the SWTP (Fig. 9h). Since the magnitude of ω_{IG} and ω_{ID} is much smaller than that of ω_Q, the AMSC forcing plays a dominant role in modulating the vertical circulation. When the AMSC is higher than normal, the anomalous vertical circulation would enhance the coupling between the mid-level convection and the upper-level divergence. The upper-level divergent circulation in the upper reaches of the SAH track would keep strengthening the SAH before June. Consequently, a stronger SAH would shift farther northwestward in June.

6 Persistence of the correlation between the AMSC and the position of the SAH in June

To identify the persistency of the AMSC in the central IO-SWTP region, we analyzed the temporal evolution of the correlations between the zonal wind and the AMSCI in spring, and between the zonal wind in spring and the SAH meridional position in June. In particular, we calculated the correlation between the 31-day running averages of the AMSCI and the zonal winds at 24°N, 80°E from 1000 to 100 hPa in spring, between the M-SAHI in June and the 31-day running average of these zonal winds, and between the Z-SAHI in June and the 31-day running average of these zonal winds. The zonal wind is analyzed here because the AMSC forcing persistently enhances the easterly wind in the southern flank of the SAH from April to May (Fig. S2). The higher apparent moisture sink in the central IO than in the SWTP leads to significant negative correlation coefficients between the 31-day running averages of the AMSCI and the zonal winds at 24°N, 80°E in early spring between 850 and 400 hPa, and above 300 hPa (Fig. 10a). Once established, these negative correlations persist until the end of May. These significant negative correlation coefficients indicate that the higher AMSCI results in stronger easterly winds between the central IO and the SWTP in March–May. The persistence is also apparent in the correlation between the meridional position of the SAH in June and the 31-day running average of the zonal winds at (24°N, 80°E) from 1000 to 100 hPa (Fig. 10b). A significant negative correlation above 200 hPa appears in mid-April and persists to late May. Similar conditions are found over 700–500 hPa. These results also indicate that anomalous easterly winds, especially those in the upper troposphere, are one of the most important factors in causing an anomalous meridional position of the SAH in June (Zhang et al. 2006; Wei et al. 2017; Ge et al. 2018a). There is also a significant correlation between the Z-SAHI in June and the 31-day running average of the zonal winds at (24°N,80°E), but it only persists until the end of April within the mid-lower troposphere (Fig. 10c).

The correlation coefficients between the meridional position of the SAH in June and the 31-day running average AMSCI are statistically significant above the 99% confidence level most of the time in spring (blue curve in Fig. 10d). Similar correlations occur between the meridional position of the SAH in June and the 31-day running average of the diabatic heating field, calculated using the apparent heat source in the central IO minus that in the SWTP (red curve in Fig. 10d). The correlation between the AMSCI and the zonal position of the SAH in June remains significant from early April to the middle of May, but a significant correlation with the apparent heat source only lasts until late April (Fig. 10e). This indicates that the AMSC is continuously linked with the SAH shift in June. The persistence of significant correlations between the AMSC, zonal wind and the SAH position in June further suggests that the three variables are physically linked. A stronger apparent moisture sink over the central IO than over the SWTP region results in anomalous easterly winds between the two regions, which

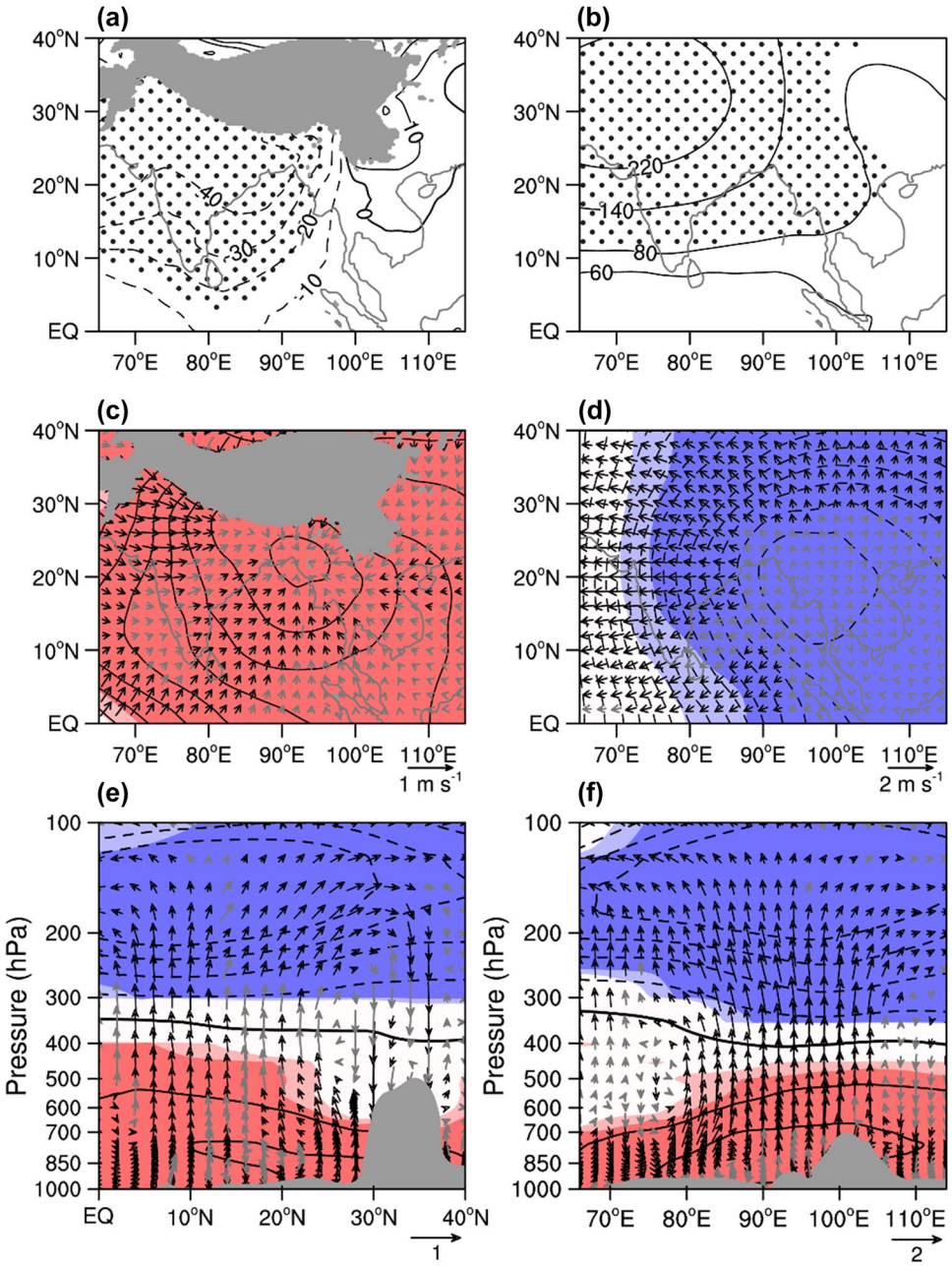

Fig. 7 Regression results of geopotential height at **a** 850 hPa and **b** 100 hPa, divergent winds at **c** 850 hPa and **d** 100 hPa, vertical divergent circulation (vector, vertical velocity is multiplied by 100) and velocity potential (contour, units: 4×10^5 m^2 s^{-1}) along **e** 80°E and **f** 24°N against the normalized AMSCI in May. The stippling in panels **a** and **b**, and the bold arrows in panels **c**–**f** denote the 95% significance based on the Student's *t* test. In panels **c**–**f**, the light and dark shadings denote the 95% and 99% significance based on the Student's *t* test, where the blue and red shadings are for negative and positive regressions coefficients, respectively. The gray areas in (**a**) and (**c**) denote the elevation threshold at 850 hPa, and the gray areas in (**e**) and (**f**) denote the surface elevation

enhances the northwestward shift of the SAH in June. When the apparent moisture sink over the central IO is weaker than that over the SWTP, the opposite occurs and the SAH is observed farther southeastward in June.

7 ECHAM6 model results

Two sensitivity experiments were conducted using the ECHAM6 model to examine the key physical processes by which the AMSC over the central IO (rectangle A in Fig. 11a) and the SWTP (rectangle B in Fig. 11a) in spring affect the northward shift of the SAH in June. Rectangles A and B are the same as those in Fig. 2. The apparent moisture sink anomalies regressed against the AMSCI in spring are used as forcing data in the sensitivity experiments. Specifically, the apparent moisture sink anomalies in the two rectangular areas are superimposed onto the modelled specific humidity from 1st March to 31st May in experiment No. 1 (EXP1), and profiles with opposite signs (Fig. 11c) are applied to experiment No. 2 (EXP2). Note that the solid curves in Fig. 11b, c represent the profile of the anomalous apparent moisture sink added in rectangle A, and the dashed curves represent the profile of anomalous apparent moisture sink added in rectangle B.

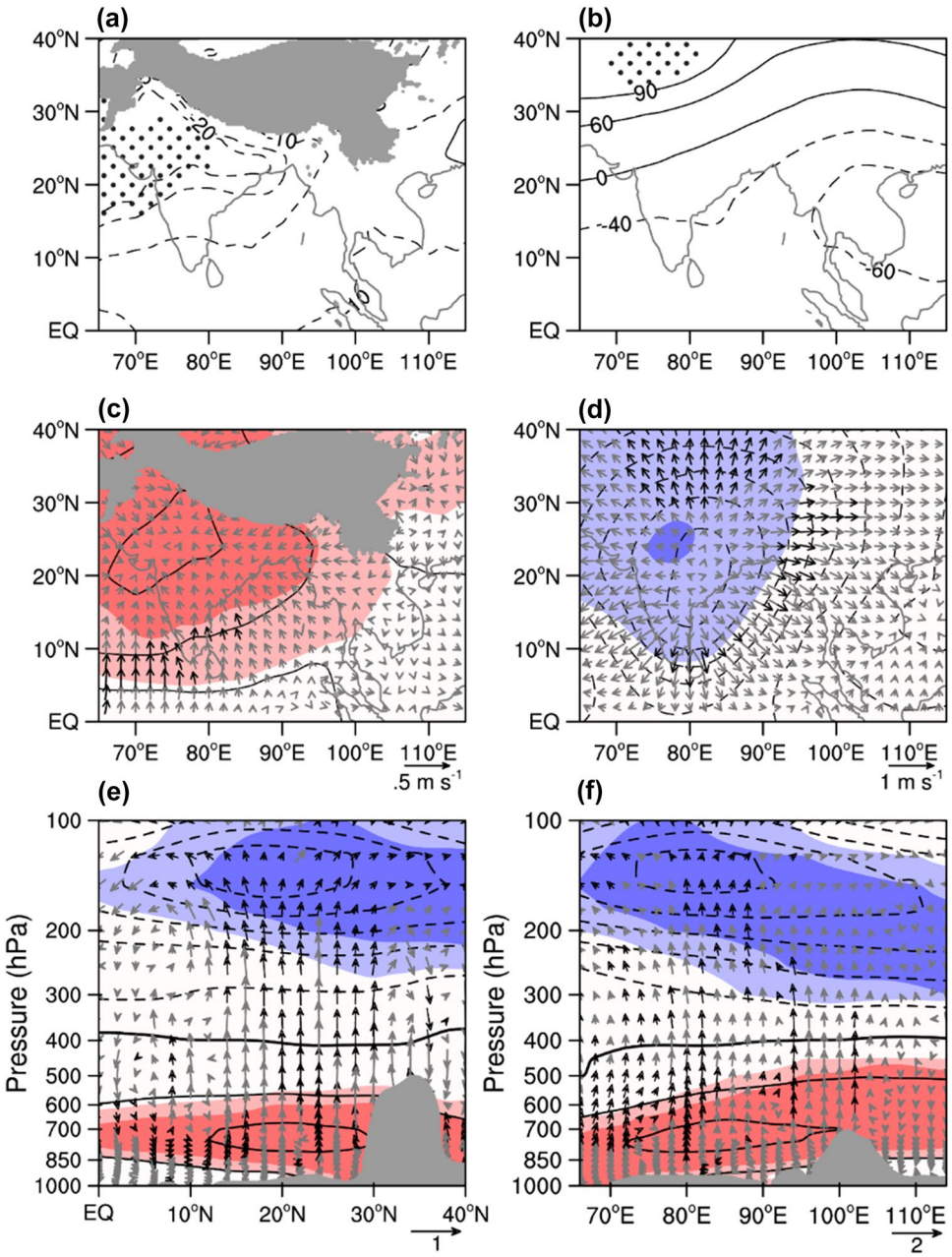

Fig. 8 Regression results of geopotential height at **a** 850 hPa and **b** 100 hPa, divergent winds at **c** 850 hPa and **d** 100 hPa, vertical divergent circulation (vector, vertical velocity is multiplied by 100) and velocity potential (contour, units: 3×10^5 m^2 s^{-1}) along **e** 80°E and **f** 24°N in June against the normalized AMSCI in April. The stippling in panels **a** and **b**, and the bold arrows in panels **c**–**f** denote the 95% significance based on the Student's *t* test. In panels **c**–**f**, the light and dark shadings denote the 95% and 99% significance based on the Student's *t* test, where the blue and red shadings are for negative and positive regressions coefficients, respectively. The gray areas in (**a**) and (**c**) denote the elevation threshold at 850 hPa, and the gray areas in (**e**) and (**f**) denote the surface elevation

The differences in the physical quantities in EXP1 from those in EXP2 are analyzed as follows.

The AMSC over the central IO-SWPT induces negative geopotential height anomalies in the lower troposphere associated with positive geopotential height anomalies in the upper troposphere (Fig. 12a, b). The divergent wind varies accordingly, with a significant low-level convergence over the central IO-SWTP and a significant upper-level divergence from eastern China to the west of India (Fig. 12c, d). The pressure-latitude section along 80°E features a pronounced low-level convergence associated with significant ascending motions around 10°N and significant upper-level divergence (Fig. 12e). In the pressure-longitude section, significant low-level convergence and upper-level divergence anomalies mainly occupy the west of 100°E (Fig. 12f).

The circulation response to the AMSC forcing grows stronger in May. For example, the low-level geopotential anomalies are more prominent than in April, whereas the upper-level geopotential anomalies largely maintain the same magnitude over the research domain (Fig. 13a, b). These changes in geopotential height are consistent with the divergent wind anomalies in the upper and lower troposphere (Fig. 13c, d). The persistent modulation of the AMSC considerably enhances the lower-level convergence and upper-level divergence over South Asia. Both the pressure-longitude and pressure-latitude cross-sections

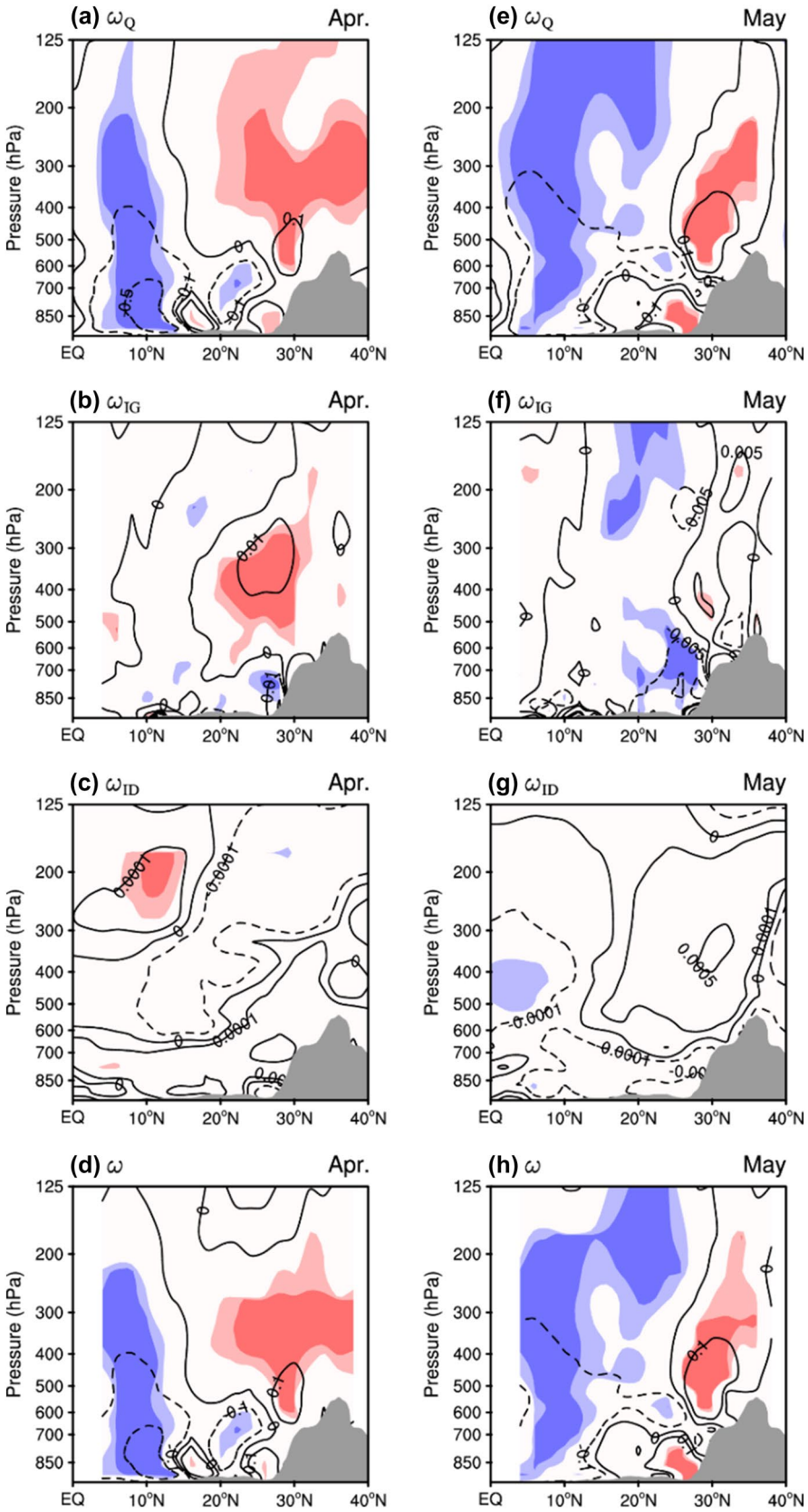

Fig. 9 Vertical structure of **a** diabatic heating component ω_Q, **b** isentropic gliding component ω_{IG}, **c** isentropic displacement component ω_{ID}, and **d** total ω forcing along 80°E in April. Panels **e**–**h** are the same as (**a**)–(**d**) except for May. Contour units are Pa s^{-1} in each plot. The light and dark shadings denote the 95% and 99% significance based on the Student's *t* test, where the blue and red shadings represent negative and positive correlation coefficients, respectively

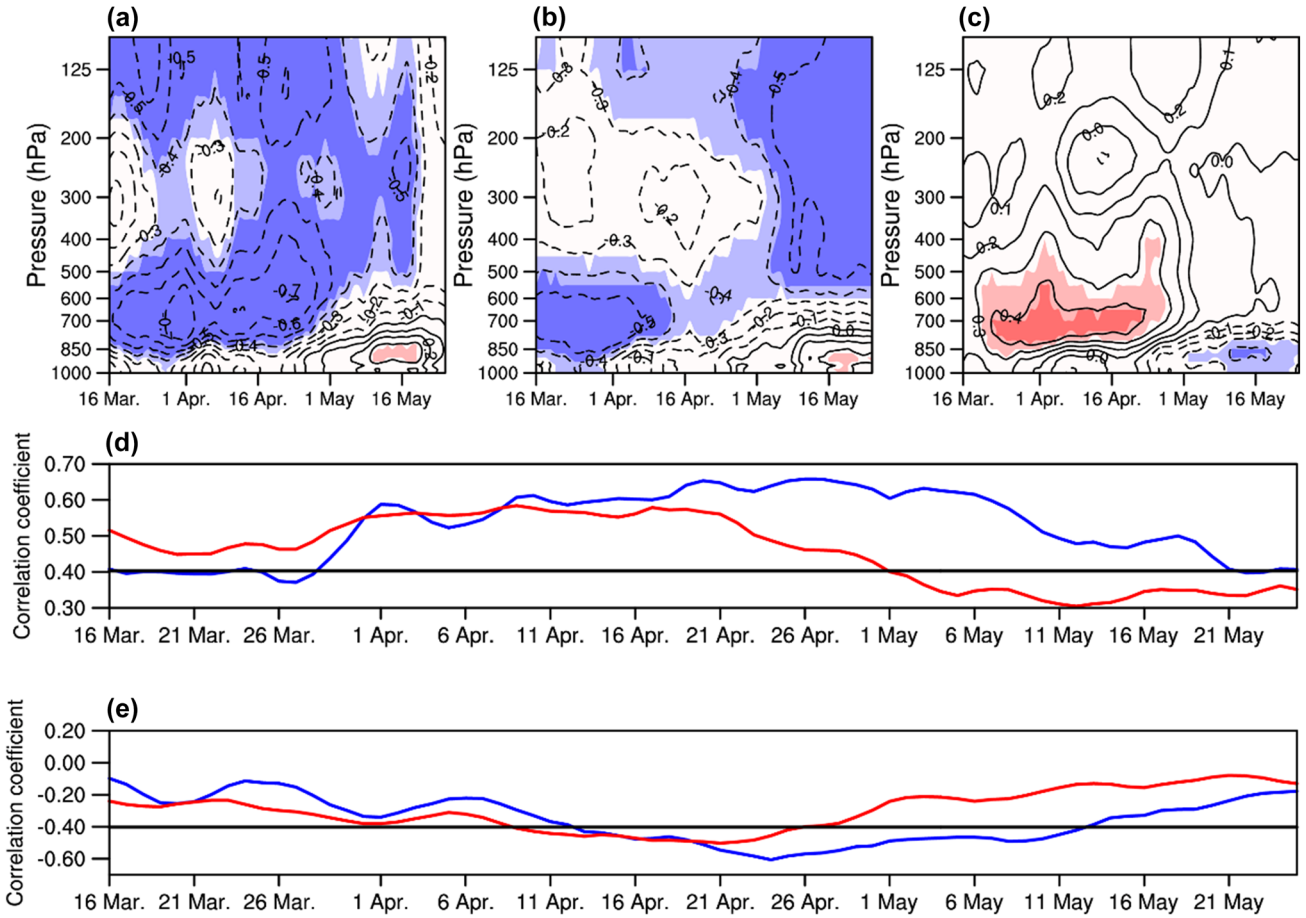

Fig. 10 **a** Correlations of the 31-day running averaged zonal winds at (24°N, 80°E) with **a** the AMSCI, **b** the M-SAHI in June, and **c** the Z-SAHI in June. **d** Correlations of the M–SAHI in June with 31-day running averaged AMSCI (blue curve) and the heating index calculated as the apparent heat source in the central IO minus that in the SWTP (red curve). (**e**) is the same as (**d**) but for the Z-SAHI in June. In panels (**a**)–(**c**), the light and dark shadings denote the 95% and 99% significance based on the Student's *t* test, where the blue and red shadings represent negative and positive correlation coefficients, respectively. In panels **d**–**e**, the dashed and solid black lines denote the threshold value of the 99% confidence level based on the Student's *t* test

show that the rising motion and upper-level divergence anomalies become more pronounced in May (Fig. 13e, f). The enhanced coupling between the low-level convergence and upper-level divergence would facilitate the development of SAH.

The anomalous circulation pattern favors the core of the SAH shifting farther northwestward in June. In fact, in June the SAH's core is (33.1°N, 62.1°E) in EXP1 but (31.6°N, 70.1°E) in EXP2. It is clear that the position of the SAH's core in June is farther northwest in EXP1 than in EXP2. The difference in the position of the SAH's core passes the significance test above the 95% confidence level in both the zonal and meridional directions. These modelled results, which reproduce the main characteristics of the observations well, indicate that the apparent moisture sink contrast of the central IO and the SWTP is one of the most important factors that influences the position of the SAH in June.

8 Summary

In this study, the meridional dipole of the spring AMSC over the region spanning the central IO and the SWTP is identified as a significant leading signal for the SAH position in June on an interannual timescale. The AMSCI is calculated as the difference in the apparent moisture sink between two key regions in spring. In 1979–2018, the correlation coefficient between the April AMSCI in the central IO-SWTP and the meridional position of the SAH's core in June, calculated from the ERA-Interim data, is 0.56, and that associated with the AMSCI in May is 0.48, with both values significant at the 99% confidence level. The significant correlation between the AMSCI and the position of the SAH's core can persist throughout the spring once it has been established in early spring. The strongly persistent correlation between the central IO-SWTP AMSCI and the position of the SAH's core in June indicates that the latent heating contrast within

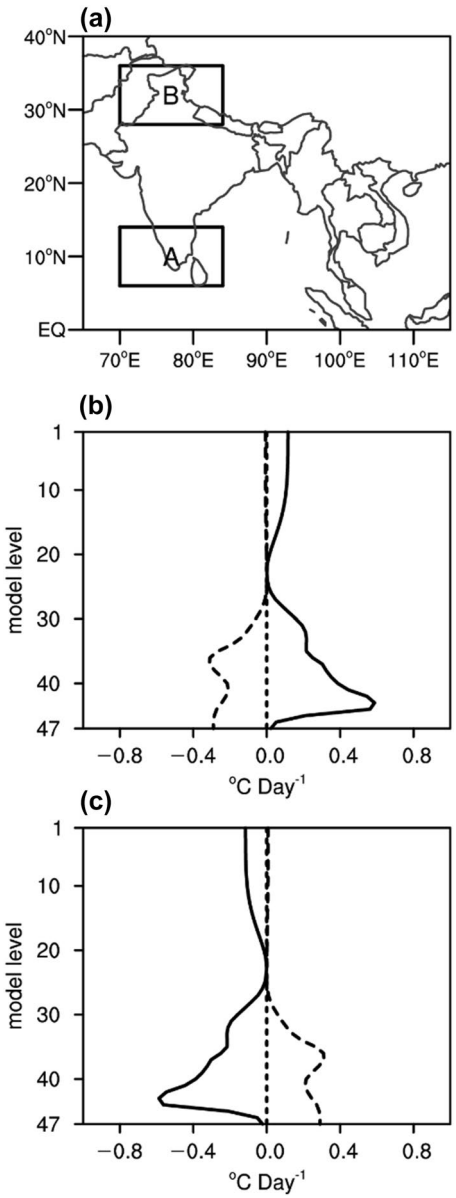

Fig. 11 **a** Spatial distribution of the apparent moisture sink forcing anomalies in the sensitivity experiments, **b** the vertical profile of the apparent moisture sink anomaly averaged in rectangle A (solid line) and rectangle B (dashed line) in EXP1 (units: °C Day^{-1}), **c** the same as (**b**) but for EXP2

the central IO-SWTP in spring has powerful potential for predicting the interannual variability of the SAH in June.

The statistical analysis and ECHAM6 model experiments further confirm that the AMSCI is a reasonable index for predicting the position of the SAH in June. The key physical processes linking the AMSC in spring and the meridional position of the SAH's core in June can be explained as follows: when the AMSC is higher than normal, the heating pattern induces anomalous vertical circulation that further enhances the coupling between the mid-level convection and the upper-level divergence. The upper-level divergent circulation occupies the upper reaches of the path along which the SAH shifts northwestward to the Tibetan Plateau. This promotes the movement of the SAH farther to the northwest in June. When the AMSC is lower than normal, it induces the opposite atmospheric response, causing the SAH to shift farther southeastward than normal in June. The modeling results obtained from the atmospheric general circulation model, ECHAM6, substantiate our hypothesis that the physical processes described above are key to the position of the SAH.

The AMSC, as part of the atmospheric internal variability, is subject to the SST anomalies in the Indo-Pacific region and even the remote SST forcing. Research suggests that the Indian Ocean Basin Mode (IOBM) is the main driver of the thermal forcing of the Tibetan Plateau in late spring (Zhao et al. 2018). The evolution of ENSO in boreal spring can also modulate the diabatic heating related to the SAH via the "atmospheric bridge" (Liu et al. 2017). The tropical Indian Ocean warming generates easterly wind anomalies that further offset the enhanced convection resulted from the local SST warming in tropical western North Pacific after spring (Lin et al. 2021). The SST configuration related to the AMSC requires further investigation. This study has focused on the correlation between the apparent moisture sink contrast in the central IO-SWTP in spring and the position of the SAH's core in June on interannual timescales. The ASM response to the global warming could change the heating pattern that further causes an interdecadal variation of the meridional position of the SAH's core (Fig. 1c) (Li et al. 2010). The physical processes behind this interdecadal variation need further investigation.

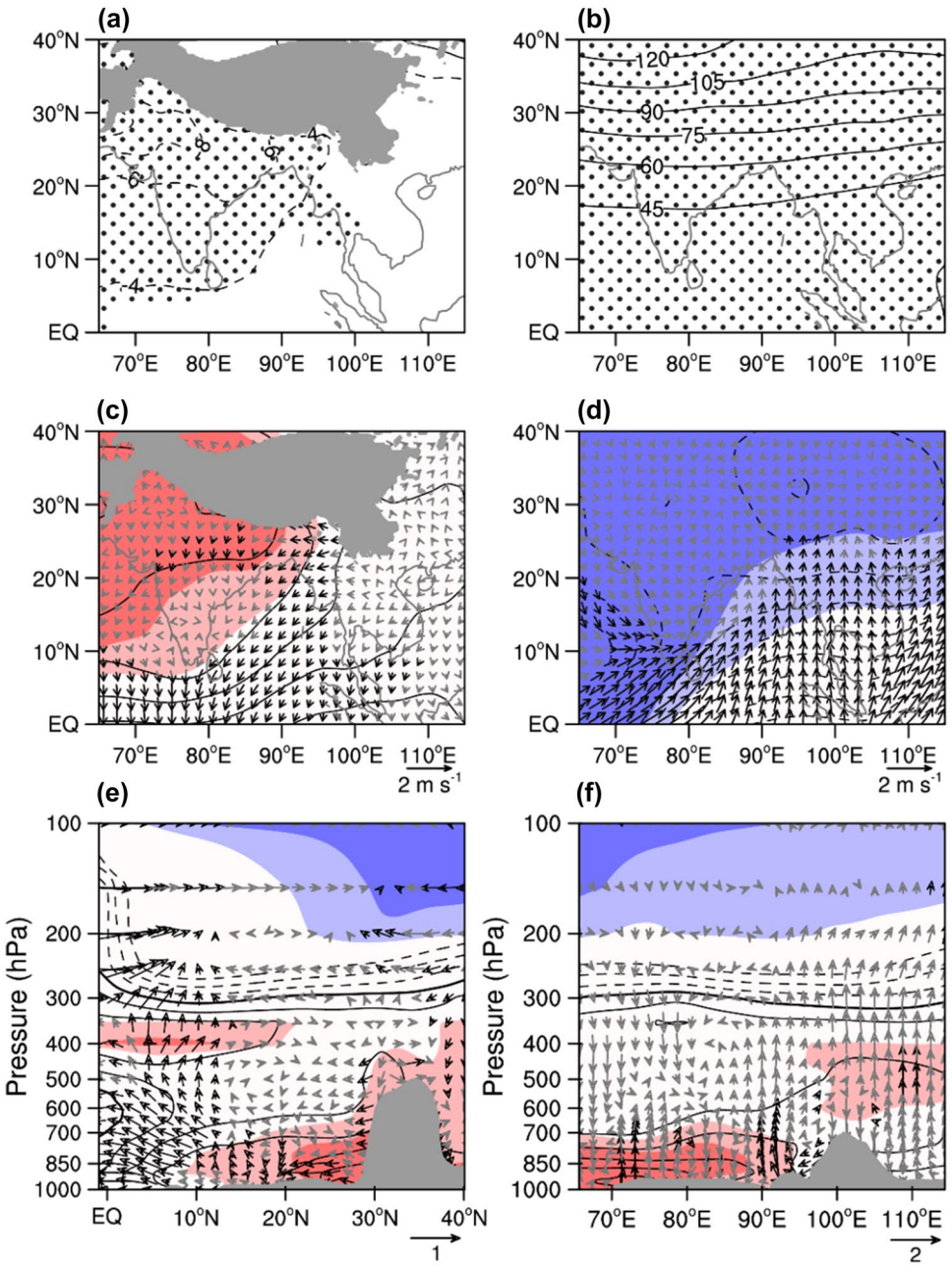

Fig. 12 The difference between EXP1 and EXP2 (EXP1 minus EXP2) in geopotential height at **a** 850 hPa and **b** 100 hPa, divergent winds (vector) and velocity potential (contour, units: 2×10^5 m^2 s^{-1}) at **c** 850 hPa and **d** 100 hPa, vertical divergent circulation (vector, vertical velocity is multiplied by 100) and velocity potential (contour, units: 2×10^5 m^2 s^{-1}) along **e** 80°E and **f** 24°N in April. The vertical velocity is multiplied by 100 in (**e**) and 10 in (**f**). The dotted areas in (**a**)–(**b**) and the bold black arrows in (**c**)–(**f**) denote the 95% significance based on the Student's *t* test. In panels (**c**)–(**f**), the light and dark shadings denote the 95% and 99% significance based on the Student's *t* test, where the blue and red shadings are for negative and positive regressions coefficients, respectively. The gray areas in (**a**) and (**c**) denote the elevation threshold at 850 hPa, and the gray areas in (**e**) and (**f**) denote the surface elevation

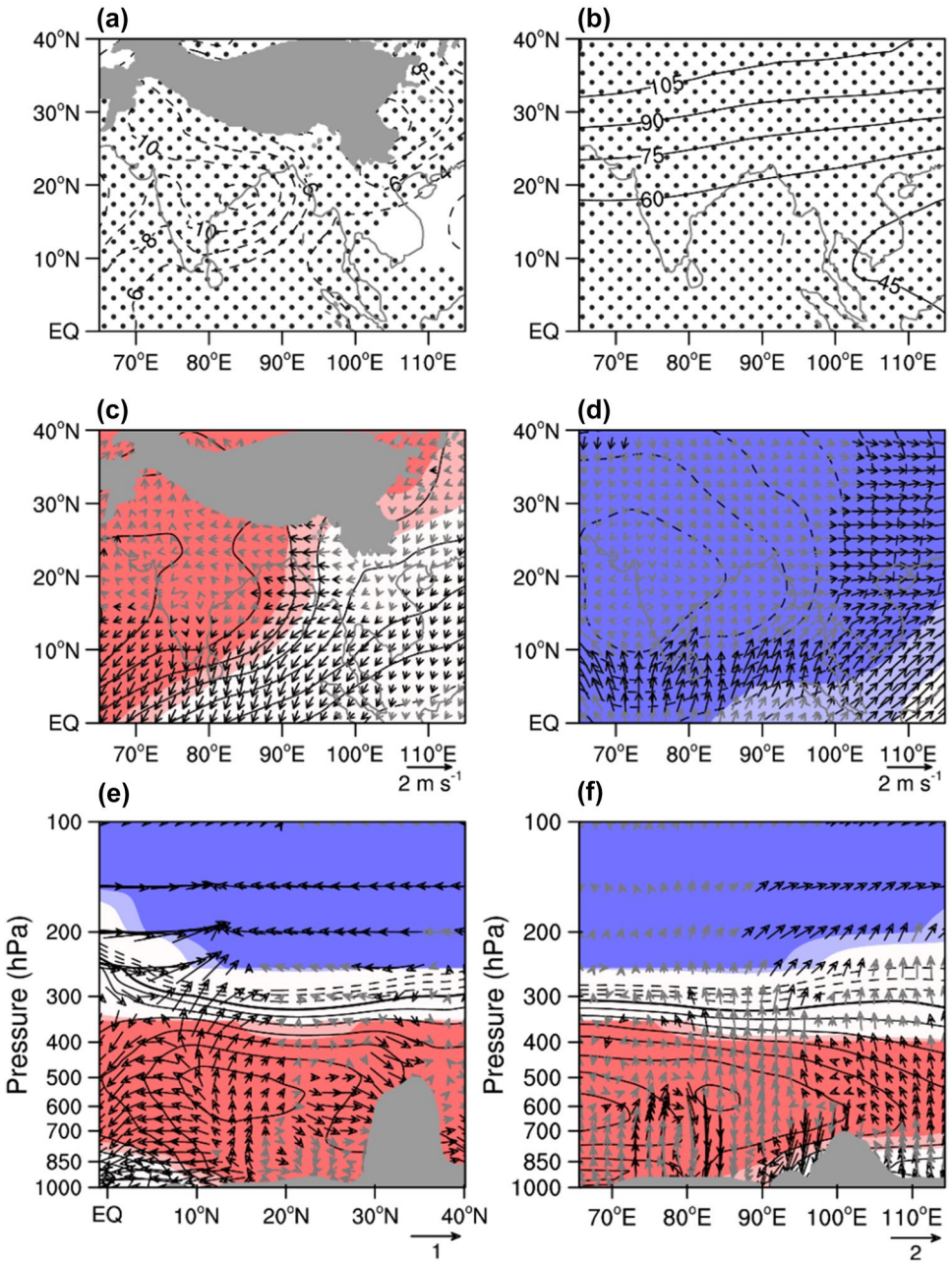

Fig. 13 The difference between EXP1 and EXP2 (EXP1 minus EXP2) in geopotential height at (**a**) 850 hPa and (**b**) 100 hPa, divergent winds (vector) and velocity potential (contour, units: 2×10^5 m^2 s^{-1}) at (**c**) 850 hPa and (**d**) 100 hPa, vertical divergent circulation (vector, vertical velocity is multiplied by 100) and velocity potential (contour, units: 2×10^5 m^2 s^{-1}) along (**e**) 80°E and (**f**) 24°N in May. The vertical velocity is multiplied by 100 in (**e**) and 10 in (**f**). The dotted areas in (**a**)–(**b**) and the bold black arrows in (**c**)–(**f**) denote the 95% significance based on the Student's *t* test. In panels (**c**)–(**f**), the light and dark shadings denote the 95% and 99% significance based on the Student's *t* test, where the blue and red shadings are for negative and positive regressions coefficients, respectively. The gray areas in (**a**) and (**c**) denote the elevation threshold at 850 hPa, and the gray areas in (**e**) and (**f**) denote the surface elevation

Supplementary Information The online version contains supplementary material available at https://doi.org/10.1007/s00382-022-06161-z.

Acknowledgements This work was supported by the National Natural Science Foundation of China (42030603, 42022035, 42005050, 41805059, 41975093 and 42105021), the program for Yunnan innovative team for climate change over Greater Mekong Subregion (2019HC027), the Natural Science Foundation of Yunnan Province (2019FY003006), and Yunnan Science and Technology Department Youth Project (202001BB050014). Four authors have equal contribution to this work. The ERA-Interim reanalysis data was downloaded from http://apps.ecmwf.int/datasets/data/interim-full-daily/levtype=pl/.

References

Cao J, Gui S, Su Q, Yang Y (2016) The variability of the Indian-East Asian summer monsoon interface in relation to the spring seesaw mode between the Indian Ocean and the Central-Western Pacific. J Clim 29:5027–5040. https://doi.org/10.1175/JCLI-D-15-0839.1

Cen S, Chen W, Chen S, Liu Y, Ma T (2020) Potential impact of atmospheric heating over East Europe on the zonal shift in the South Asian high: the role of the silk road teleconnection. Sci Rep 10:6543. https://doi.org/10.1038/s41598-020-63364-2

Cheng Y, Fan G, Zhang Y, Lai X (2018) Analysis of vertical temperature gradient characteristics and its causes over Qinghai-Tibetan plateau and its surroundings. Plateau Meteorol 37:333–348

Choi J-W, Kim B-J, Zhang R, Nam J-C, Park K-J, Kim J-Y, Kim D-W (2015) Possible influence of South Asian high on summer rainfall variability in Korea. Clim Dyn 46:833–846. https://doi.org/10.1007/s00382-015-2615-0

Dee D et al (2011) The ERA-Interim reanalysis: configuration and performance of the data assimilation system. Q J R Meteorol Soc 137:553–597. https://doi.org/10.1002/qj.828

Ge J, You Q, Zhang Y (2018a) The influence of the Asian summer monsoon onset on the northward movement of the South Asian high towards the Tibetan Plateau and its thermodynamic mechanism. Int J Climatol 38:543–553. https://doi.org/10.1002/joc.5192

Ge J, You Q, Zhang Y (2018b) Interannual variation of the northward movement of the South Asian High towards the Tibetan Plateau and its relation to the Asian Summer Monsoon onset. Atmos Res 213:381–388. https://doi.org/10.1016/j.atmosres.2018.06.026

Gui S, Yang R, Cao J, Huang W (2020) Precipitation over East Asia simulated by ECHAM6.3 with different schemes of cumulus convective parameterization. Clim Dyn 54:4233–4261. https://doi.org/10.1007/s00382-020-05226-1

Han Y et al (2021) Impacts of the Silk Road pattern on the interdecadal variations of the atmospheric heat source over the Tibetan Plateau. Atmos Res. https://doi.org/10.1016/j.atmosres.2021.105696

He J, Wen M, Wang L, Xu H (2006) Characteristics of the onset of the Asian summer monsoon and the importance of Asian-Australian "land bridge." Adv Atmos Sci 23:951–963. https://doi.org/10.1007/s00376-006-0951-z

Huang G, Qu X, Hu K (2011) The impact of the tropical Indian Ocean on South Asian high in boreal summer. Adv Atmos Sci 28:421–432. https://doi.org/10.1007/s00376-010-9224-y

Kinne S et al (2013) HAC-v1: a new global aerosol climatology for climate studies. J Adv Model Earth Syst. https://doi.org/10.1002/jame.20035

Krishnamurti TN, Daggupaty SM, Fein J, Kanamitsu M, Lee JD (1973) Tibetan high and upper tropospheric tropical circulations during northern summer. Bull Am Meteor Soc 54:1234–1250. https://doi.org/10.1175/1520-0477-54.12.1234

Krishnamurti TN, Bedi HS, Subramaniam M (1989) The summer monsoon of 1987. J Climate 2:321–340

Li J, Wu Z, Jiang Z, He J (2010) Can global warming strengthen the East Asian summer monsoon? J Clim 23:6696–6705. https://doi.org/10.1175/2010JCLI3434.1

Li H, He S, Fan K, Wang H (2019) Relationship between the onset date of the Meiyu and the South Asian anticyclone in April and the related mechanisms. Clim Dyn 52:209–226. https://doi.org/10.1007/s00382-018-4131-5

Lin S, Yang S, He S, Li Z, Chen J, Dong W, Wu J (2021) Attribution of the seasonality of atmospheric heating changes over the western tropical Pacific with a focus on the spring season. Clim Dyn. https://doi.org/10.1007/s00382-021-06020-3

Liu Y, Wu G (2004) Progress in the study on the formation of the summertime subtropical anticyclone. Adv Atmos Sci 21:322–342. https://doi.org/10.1007/BF02915562

Liu Y, Wu G, Liu H, Liu P (2001) Condensation heating of the Asian summer monsoon and the subtropical anticyclone in the Eastern Hemisphere. Clim Dyn 17:327–338. https://doi.org/10.1007/s003820000117

Liu B, Wu G, Mao J, He J (2013) Genesis of the south Asian high and its impact on the Asian summer monsoon onset. J Clim 26:2976–2991. https://doi.org/10.1175/JCLI-D-12-00286.1

Liu B, Zhu C, Yuan Y (2017) Two interannual dominant modes of the South Asian High in May and their linkage to the tropical SST anomalies. Clim Dyn 49:2705–2720. https://doi.org/10.1007/s00382-016-3490-z

Luo S, Qian Z, Wang Q (1982) The climatic and synoptical study about the relation between the Qinhai-Xizang high pressure on the 100 hPa surface and the flood and drought in east China in summer. Plateau Meteorol 1:1–10

Ma L, Jiang Z (2020) Improved leading modes of interannual variability of the Asian-Australian monsoon in an AGCM via incorporating a stochastic multicloud model. Clim Dyn 54:759–775. https://doi.org/10.1007/s00382-019-05025-3

Mlawer E, Taubman S, Brown P, Iacono M, Clough S (1997) Radiative transfer for inhomogeneous atmospheres: RRTM, a validated correlated-k model for the longwave. J Geophys Res 102:16663–16682. https://doi.org/10.1029/97JD00237

Ning L, Liu J, Wang B (2017) How does the South Asian high influence extreme precipitation over eastern China? J Geophys Res Atmos 122:4281–4298. https://doi.org/10.1002/2016JD026075

Nordeng T (1994) Extended versions of the convective parametrization scheme at ECMWF and their impact on the mean and transient activity of the model in the tropics. ECMWF Tech Memo 206

Nordling K et al (2019) Role of climate model dynamics in estimated climate responses to anthropogenic aerosols. Atmos Chem Phys 19:9969–9987. https://doi.org/10.5194/acp-19-9969-2019

Nützel M, Dameris M, Garny H (2016) Movement, drivers and bimodality of the South Asian high. Atmos Chem Phys 16:14755–14774. https://doi.org/10.5194/acp-16-14755-2016

Qian Y, Zhang Q, Yao Y, Zhang X (2002) Seasonal variation and heat preference of the south Asia high. Adv Atmos Sci 19:821–836. https://doi.org/10.1007/s00376-002-0047-3

Qu X, Huang G (2012) An enhanced influence of tropical Indian Ocean on the South Asia high after the late 1970s. J Clim 25:6930–6941. https://doi.org/10.1175/JCLI-D-11-00696.1

Rackow T, Goessling H, Jung T, Sidorenko D, Semmler T, Barbi D, Handorf D (2018) Towards multi-resolution global climate modeling with ECHAM6-FESOM. Part II: climate variability. Clim Dyn. https://doi.org/10.1007/s00382-016-3192-6

Raman CRV, Rao YP (1981) Blocking highs over Asia and monsoon droughts over India. Nature 289:271–273

Randel W, Park M (2006) Deep convective influence on the Asian summer monsoon anticyclone and associated tracer variability observed with Atmospheric Infrared Sounder (AIRS). J Geophys Res. https://doi.org/10.1029/2005JD006490

Reick C, Raddatz T, Brovkin V, Gayler V (2013) Representation of natural and anthropogenic land cover change in MPI-ESM. J Adv Model Earth Syst. https://doi.org/10.1002/jame.20022

Reiter E, Gao D-Y (1982) Heating of the Tibet plateau and movements of the South Asian high during spring. Mon Weather Rev. https://doi.org/10.1175/1520-0493(1982)110%3c1694:HOTTPA%3e2.0.CO;2

Roeckner E, Mauritsen T, Esch M, Brokopf R (2012) Impact of melt ponds on Arctic sea ice in past and future climates by MPI-ESM. J Adv Model Earth Syst. https://doi.org/10.1029/2012MS000157

Shi J, Qian W (2016) Connection between anomalous zonal activities of the south Asian high and Eurasian summer climate anomalies. J Clim. https://doi.org/10.1175/JCLI-D-15-0823.1

Stevens B et al (2013) Atmospheric component of the MPI-M earth system model: ECHAM6. J Adv Model Earth Syst 5. https://doi.org/10.1002/jame.20015

Tao S, Chen L (1987) A review of recent research on the East Asian-summer monsoon in China. In: Krishnamurti TN (ed) Monsoon meteorology. Oxford University Press, Oxford, pp 60–92

Wang S, Qian Y (2000) Diagnostic study of apparent heat sources and moisture sinks in the south china sea and its adjacent areas during the onset of 1998 SCS monsoon. Adv Atmos Sci 17:285–298. https://doi.org/10.1007/s00376-000-0010-0

Wang L, Dai A, Guo S, Ge J (2017) Establishment of the South Asian high over the Indo-China Peninsula during late spring to summer. Adv Atmos Sci 34:169–180. https://doi.org/10.1007/s00376-016-6061-7

Wang M, Guo D, Zhong S (2019) Comparison of the multi-source datasets in calculation of the atmospheric heat sources over the Tibetan plateau. Meteorol Mon 45:1718–1726

Wei W, Zhang R, Wen M (2012) Meridional variation of South Asian high and its relationship with the summer precipitation over China (in Chinese). J Appl Meteorol Sci 23:650–659

Wei W, Zhang R, Wen M, Rong X, Li T (2013) Impact of Indian summer monsoon on the South Asian high and its influence on summer rainfall over China. Clim Dyn 43:1257–1269. https://doi.org/10.1007/s00382-013-1938-y

Wei W, Zhang R, Wen M, Kim B-J, Nam J-C (2015) Interannual variation of the South Asian high and its relation with Indian and East Asian summer monsoon rainfall. J Clim 28:2623–2634. https://doi.org/10.1175/JCLI-D-14-00454.1

Wei W, Zhang R, Wen M, Yang S (2017) Relationship between the Asian westerly jet stream and summer rainfall over Central Asia and North China: roles of the Indian monsoon and the South Asian high. J Clim 30:537–552. https://doi.org/10.1175/JCLI-D-15-0814.1

Wei W, Zhang R, Yang S, Li W, Wen M (2019) Quasi-biweekly oscillation of the south Asian high and its role in connecting the Indian and East Asian summer rainfalls. Geophys Res Lett 46:14742–14750. https://doi.org/10.1029/2019GL086180

Wu G, Liu Y (2003) Summertime quadruplet heating pattern in the subtropics and the associated atmospheric circulation. Geophys Res Lett 30:5–1. https://doi.org/10.1029/2002GL016209

Wu H, Yang K, Niu X, Chen Y (2015) The role of cloud height and warming in the decadal weakening of atmospheric heat source over the Tibetan Plateau. Sci China Earth Sci 58:395–403. https://doi.org/10.1007/s11430-014-4973-6

Wu G, Ma T, Liu Y, Jiang Z (2020) PV-Q perspective of cyclogenesis and vertical velocity development downstream of the Tibetan Plateau. J Geophys Res Atmos 125:e2019JD030912. https://doi.org/10.1029/2019JD030912

Xue X, Chen W (2019) Distinguishing interannual variations and possible impacted factors for the northern and southern mode of South Asia High. Clim Dyn. https://doi.org/10.1007/s00382-019-04837-7

Xue X, Chen W, Chen S, Zhou D (2015) Modulation of the connection between boreal winter ENSO and the South Asian high in the following summer by the stratospheric Quasi-Biennial Oscillation. J Geophys Res Atmos. https://doi.org/10.1002/2015JD023260

Xue X, Chen W, Chen S (2017) The climatology and interannual variability of the South Asia high and its relationship with ENSO in CMIP5 models. Clim Dyn 48:3507–3528. https://doi.org/10.1007/s00382-016-3281-6

Xue X, Chen W, Chen S, Feng J (2018) PDO modulation of the ENSO impact on the summer South Asian high. Clim Dyn 50:1393–1411. https://doi.org/10.1007/s00382-017-3692-z

Yanai M, Li C, Song Z (1992) Seasonal heating of the Tibetan Plateau and its effects on the evolution of the Asian summer monsoon. J Meteorol Soc Jpn 79:419–434. https://doi.org/10.2151/jmsj1965.70.1B_319

Yang R, Xie Z, Cao J (2017) A Dynamic index for the westward ridge point variability of the western pacific subtropical high during summer. J Clim 30:3325–3341. https://doi.org/10.1175/JCLI-D-16-0434.1

Yang R, Gui S, Cao J (2019) Bay of Bengal-East Asia-Pacific teleconnection in boreal summer. J Geophys Res Atmos 124:4395–4412. https://doi.org/10.1029/2019JD030332

Yin Y, Han C, Yang G, Huang Y, Liu M, Wang X (2020) Changes in the summer extreme precipitation in the Jianghuai plum rain area and their relationship with the intensity anomalies of the south Asian high. Atmos Res 236:104793. https://doi.org/10.1016/j.atmosres.2019.104793

Zhang Q, Wu G (2001) The large area flood and drought over Yangtze River valley and its relation to the South Asia High (in Chinese)

Zhang P, Song Y, Vernon EK (2005) South Asian high and Asian-Pacific-American climate teleconnection. Adv Atmos Sci 22:915–923. https://doi.org/10.1007/BF02918690

Zhang B, Liang J, Lin A, Li C, Gu D (2006) Frontal rain and summer monsoon rain during pre-rainy season in South China. Part I: determination of the division dates. Chin J Atmos Sci 30:1207–1216

Zhang P, Liu Y, He B (2015) Impact of east Asian summer monsoon heating on the interannual variation of the South Asian high. J Clim 29:151106072625005. https://doi.org/10.1175/JCLI-D-15-0118.1

Zhang H, Li W, Li W (2019a) Influence of late springtime surface sensible heat flux anomalies over the Tibetan and Iranian Plateaus on the location of the South Asian high in early summer. Adv Atmos Sci 36:93–103. https://doi.org/10.1007/s00376-018-7296-2

Zhang Y, Li J, Xue J, Zheng F, Wu R, Ha K-J, Feng J (2019b) The relative roles of the South China Sea summer monsoon and ENSO in the Indian Ocean dipole development. Clim Dyn 53:6665–6680. https://doi.org/10.1007/s00382-019-04953-4

Zhang Y, Li J, Zhao S, Zheng F, Feng J, Li Y, Xu Y (2020) Indian Ocean tripole mode and its associated atmospheric and oceanic processes. Clim Dyn 55:1367–1383. https://doi.org/10.1007/s00382-020-05331-1

Zhang S, Liu S, Zhang T (2021) Construction of the apparent moisture sink index for the movement of the South Asian high and associated indicative significance. Atmos Ocean 59:15–28. https://doi.org/10.1080/07055900.2021.1877106

Zhao Y, Duan A, Wu G (2018) Interannual variability of late-spring circulation and diabatic heating over the Tibetan Plateau associated with Indian Ocean forcing. Adv Atmos Sci 35:927–941. https://doi.org/10.1007/s00376-018-7217-4

Zhou NF, Yu Y, Qian Y (2006) Simulations of the 100-hPa South Asian high and precipitation over East Asia with IPCC coupled GCMs. Adv Atmos Sci 23:375–390

Zhu F, Lu L, Chen X, Zhao W (1980) The South Asia high. Science Press, Beijing (in Chinese)